

The first stars: formation of binaries and small multiple systems

Athena Stacy^{1,2*}, Thomas H. Greif^{3,4} and Volker Bromm^{1,2}

¹*Department of Astronomy, University of Texas, Austin, TX 78712, USA*

²*Texas Cosmology Center, University of Texas, Austin, TX 78712, USA*

³*Institut für theoretische Astrophysik, Albert-Ueberle Strasse 2, 69120 Heidelberg, Germany*

⁴*Fellow of the International Max Planck Research School for Astronomy and Cosmic Physics at the University of Heidelberg*

9 November 2018

ABSTRACT

We investigate the formation of metal-free, Population III (Pop III), stars within a minihalo at $z \simeq 20$ with a smoothed particle hydrodynamics (SPH) simulation, starting from cosmological initial conditions. Employing a hierarchical, zoom-in procedure, we achieve sufficient numerical resolution to follow the collapsing gas in the center of the minihalo up to number densities of 10^{12} cm^{-3} . This allows us to study the protostellar accretion onto the initial hydrostatic core, which we represent as a growing sink particle, in improved physical detail. The accretion process, and in particular its termination, governs the final masses that were reached by the first stars. The primordial initial mass function (IMF), in turn, played an important role in determining to what extent the first stars drove early cosmic evolution. We continue our simulation for 5000 yr after the first sink particle has formed. During this time period, a disk-like configuration is assembled around the first protostar. The disk is gravitationally unstable, develops a pronounced spiral structure, and fragments into several other protostellar seeds. At the end of the simulation, a small multiple system has formed, dominated by a binary with masses $\sim 40 M_{\odot}$ and $\sim 10 M_{\odot}$. If Pop III stars were to form typically in binaries or small multiples, the standard model of primordial star formation, where single, isolated stars are predicted to form in minihaloes, would have to be modified. This would have crucial consequences for the observational signature of the first stars, such as their nucleosynthetic pattern, and the gravitational-wave emission from possible Pop III black-hole binaries.

Key words: cosmology: theory – early Universe – galaxies: formation – stars: formation.

1 INTRODUCTION

How did the cosmic dark ages end, and how was the homogeneous early Universe transformed into the highly complex state that we observe today (e.g. Barkana & Loeb 2001; Miralda-Escudé 2003; Ciardi & Ferrara 2005)? One of the key questions is to understand the formation and properties of the first stars, the so-called Population III (or Pop III), since they likely played a crucial role in driving early cosmic evolution (e.g. Bromm & Larson 2004; Glover 2005; Bromm et al. 2009). For instance, the radiation from the first stars contributed to the reionization of the intergalactic medium (IGM), at least during its initial phase (e.g. Kitayama et al. 2004; Sokasian et al. 2004; Whalen et al. 2004; Alvarez et al. 2006; Johnson et al. 2007). After the first stars exploded as

supernovae (SNe) they spread heavy elements through the IGM, thereby providing the initial cosmic metal enrichment (e.g. Madau et al. 2001; Mori et al. 2002; Bromm et al. 2003; Wada & Venkatesan 2003; Norman et al. 2004; Greif et al. 2007; Tornatore et al. 2007). The resulting metallicity was likely crucial in governing the transition from early high-mass star formation to the normal-mass star formation seen today (e.g. Omukai 2000; Bromm et al. 2001; Schneider et al. 2002; Bromm & Loeb 2003; Frebel et al. 2007, 2009; Smith & Sigurdsson 2007).

The extent to which the radiation and metal enrichment from the first stars influenced the early Universe is largely determined by their mass. Currently, Pop III stars are believed to have first formed around $z \sim 20$ within minihaloes of mass $M \sim 10^6 M_{\odot}$ (e.g. Haiman et al. 1996; Tegmark et al. 1997; Yoshida et al. 2003). The potential wells of these minihaloes are provided by dark matter (DM), which

* E-mail: minerva@@astro.as.utexas.edu

serve to initially gather primordial gas into them. This is in contrast to present-day star-forming giant molecular clouds (GMCs), which are of similar mass to minihaloes, but which form within much larger galaxies and are not DM dominated. Previous three-dimensional simulations (e.g. Abel et al. 2002; Bromm et al. 2002) have studied the formation of $M \sim 1000 M_\odot$ prestellar cores with sizes < 0.5 pc within such minihaloes. The density in these cores is similar to those in present-day ones, but having considerably higher temperature (~ 200 K for primordial cores versus $10 - 15$ K for those within GMCs).

The mass of the first stars depends on the further evolution of such cores. Similar to present-day star formation (e.g. McKee & Tan 2002), it is expected that some of the gas within these cores will gravitationally collapse into one or more protostars of initial mass $\sim 5 \times 10^{-3} M_\odot$ (Omukai & Nishi 1998; Yoshida et al. 2008). A fraction of the core mass will be accreted onto the protostar(s), ultimately forming stars much more massive than the initial seeds. Three-dimensional simulations which studied the growth of a primordial protostar through accretion imply that the first stars were quite massive, finding an upper limit of $\sim 500 M_\odot$ (Bromm & Loeb 2004). Some of the earliest studies of Pop III star formation, however, predicted that Pop III stellar masses might be quite low, $< 1 M_\odot$ (e.g. Kashlinsky & Rees 1983). These authors emphasized the importance of angular momentum in determining the mass of Pop III stars, predicting that rotational effects would cause the primordial gas clouds to collapse into a dense disk. Only after the disk cooled to ~ 1000 K through H_2 line emission could fragmentation occur. Depending on the spin of the cloud, the fragments thus formed could have had masses as low as $\lesssim 0.2 M_\odot$. Later studies by Saigo et al. (2004) also found that high initial angular momentum would allow primordial clouds to form disks, and they further predicted that disk fragmentation into binaries would be common. Similar calculations by Machida et al. (2008), which were initialized at much lower densities and therefore at an earlier point in the gas collapse, found fragmentation would occur even for primordial gas clouds with very modest initial angular momentum. However, none of the above-mentioned investigations were initialized on cosmological scales.

Our goal in this study is to further improve our understanding of how a Pop III star is assembled through the process of accretion within the first minihaloes. More specifically, we aim to determine the final masses reached by the first stars, and whether the gas within a host minihalo forms a single star or fragments into a binary or small multiple system. To this end we perform a three-dimensional cosmological simulation that follows the formation of a minihalo with very high numerical resolution, allowing us to trace the evolution of its gas up to densities of 10^{12} cm^{-3} . Unlike the study of Bromm & Loeb (2004), which employed a constrained initialization technique on scales of ~ 150 pc, our simulation is initialized on cosmological scales. This allows the angular momentum of the minihalo to be found self-consistently, eliminating the need for an assumed spin parameter. In a fashion similar to Bromm & Loeb (2004), we represent high-density peaks that are undergoing gravitational runaway collapse with sink particles, allowing us to follow the mass flow onto the sinks well beyond the onset of collapse.

The recent simulation by Turk et al. (2009), starting from cosmological initial conditions, has shown fragmentation and the formation of two high-density peaks, which are interpreted as seeds for a Pop III binary. These peaks are similar to the multiple sinks found in our simulation. Although Turk et al. employed even higher numerical resolution, they were able to follow the evolution of the high-density peaks for only ~ 200 yr. Our sink particle method, on the other hand, enabled us to continue our calculation for several thousand years after initial runaway collapse. We could thus follow the subsequent disk evolution and further fragmentation in detail, rendering our study ideally complementary to their work.

The structure of our paper is as follows. In Section 2, we discuss the basic physical ingredients determining the accretion flow, whereas we describe our numerical methodology in Section 3. We proceed to present our results (Section 4), and conclude in Section 5.

2 PHYSICAL INGREDIENTS

2.1 Protostellar accretion

Unlike the gas from which present-day stars are formed, which can typically cool to ~ 10 K, primordial gas contained no metals and could only cool down to ~ 100 K through H_2 and HD line transitions. These elevated temperatures lead to a higher accretion rate, which can be estimated on dimensional grounds by assuming that the Jeans mass is infalling at the free-fall rate, resulting in

$$\dot{M} \simeq \frac{c_s^3}{G} \propto T^{3/2}, \quad (1)$$

where c_s is the soundspeed. This is quite close to the Shu (1977) similarity solution for collapse of a singular isothermal sphere, which gives $\dot{M} = 0.975 c_s^3 / G$. The Shu solution begins with an isothermal cloud with $\rho \propto r^{-2}$ and initially negligible infall velocities. The solution then describes the subsequent ‘inside-out’ collapse of the cloud, which physically corresponds to accretion of mass onto the central protostar. The earlier similarity solution of Larson (1969) and Penston (1969) described the collapse of an initially uniform cloud into a peaked structure with an r^{-2} density profile. This solution was later expanded by Hunter (1977) to capture the evolution after the initial formation of a hydrostatic core when it grows via accretion of the envelope. At the point of initial protostar formation, corresponding to when the central density becomes infinite in the similarity solution, the infall velocity is already 3.3 times the sound speed, and the accretion rate grows to 48 times higher than that found in Shu collapse (Hunter 1977).

In our simulation, the collapse of the gas from initially more uniform densities can be expected to behave similarly to a Larson-Penston-type solution (e.g. Omukai & Nishi 1998). The following accretion of this gas onto the central hydrostatic core should proceed from the ‘inside-out’ at rates similar to those found in the Shu and Larson-Penston-Hunter solutions.

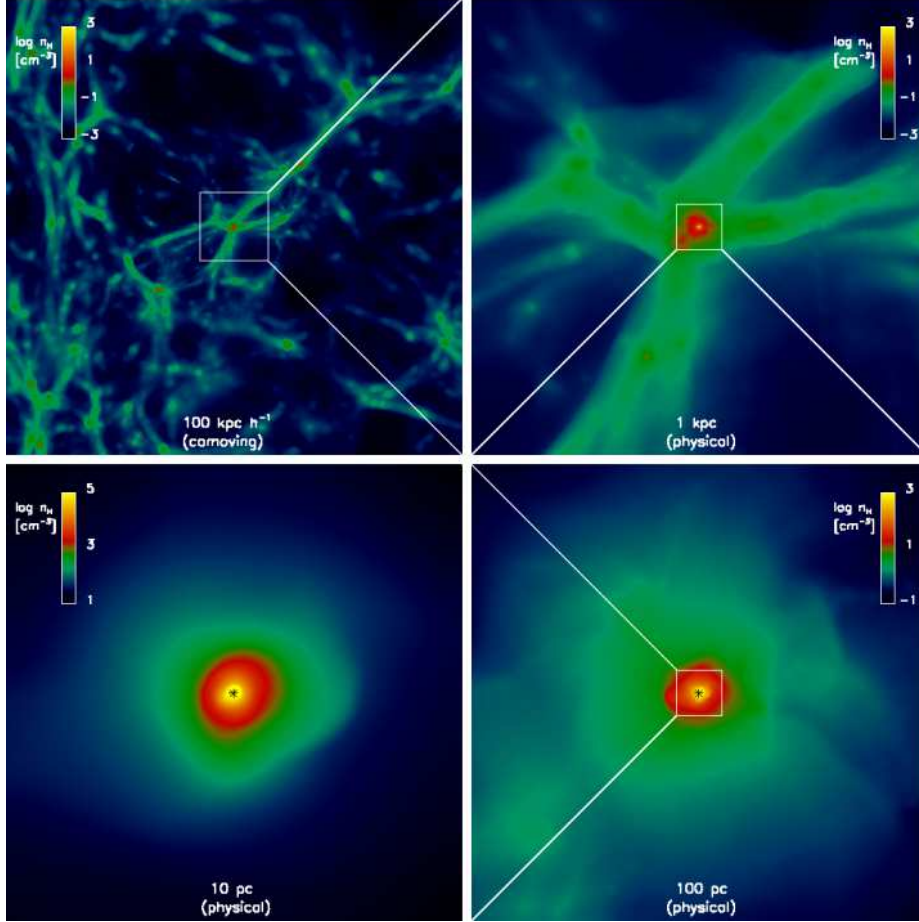


Figure 1. Final simulation output shown in density projection along the x-z plane on progressively smaller scales, as labeled on each panel. White boxes denote the region to be depicted in the next-smallest scale. In the bottom two panels, the asterisk denotes the location of the first sink formed. *Top left:* Entire simulation box. *Top right:* Minihalo and surrounding filamentary structure. *Bottom right:* Central 100 pc of minihalo. *Bottom left:* Central 10 pc of minihalo. Note how the morphology approaches an increasingly smooth, roughly spherical distribution on the smallest scales, where the gas is in quasi-hydrostatic equilibrium, just prior to the onset of runaway collapse.

2.2 Protostellar feedback effects

As the protostellar mass grows through accretion, feedback from photoionization, heating, and radiation pressure will begin to have important effects on the accretion flow and may set the upper mass limit for both present-day and primordial stars. One important difference between feedback in primordial and present-day massive star formation is due to the existence of dust grains in the latter case. For instance, Ripamonti et al. (2002) found with their one-dimensional calculations that Pop III protostellar radiation pressure will not affect the initial collapse and early stages of accretion due to the low opacity of the infalling gas. In contrast, for present-day star formation the increased opacity from dust enhances the radiation pressure and can halt infall onto stars of more than a few tens of solar masses without further mechanisms to alleviate the radiative force (see summary in McKee & Ostriker 2007). On the other hand, later in the life of a present-day star, dust absorption of ionizing photons will alter the evolution of the H II region around the star, thus reducing the photoionization feedback.

Omukai & Palla (2003) performed a detailed study of spherical accretion of metal-free gas onto a growing hydrostatic core. In this case, electron scattering is the major source of opacity determining the Eddington luminosity L_{EDD} and the critical accretion rate \dot{M}_{crit} , above which the protostellar luminosity exceeds L_{EDD} before the protostar reaches the zero-age main sequence (ZAMS), disrupting further accretion. As estimated in Bromm & Loeb (2004), if we assume the protostellar luminosity before the onset of hydrogen burning is approximately the accretion luminosity, $L_{\text{acc}} \simeq GM_*\dot{M}/R_*$, and set this luminosity equal to L_{EDD} , we find that

$$\dot{M}_{\text{crit}} \simeq \frac{L_{\text{EDD}} R_*}{GM_*} \sim 5 \times 10^{-3} \text{ M}_{\odot} \text{ yr}^{-1}, \quad (2)$$

where $R_* \sim 5 R_{\odot}$ (Bromm et al. 2001). This approximation is quite close to that found in the calculations of Omukai & Palla (2003). It should be noted that initial accretion rates higher than \dot{M}_{crit} are possible since protostars begin with much larger radii and only gradually shrink during Kelvin-Helmholtz contraction.

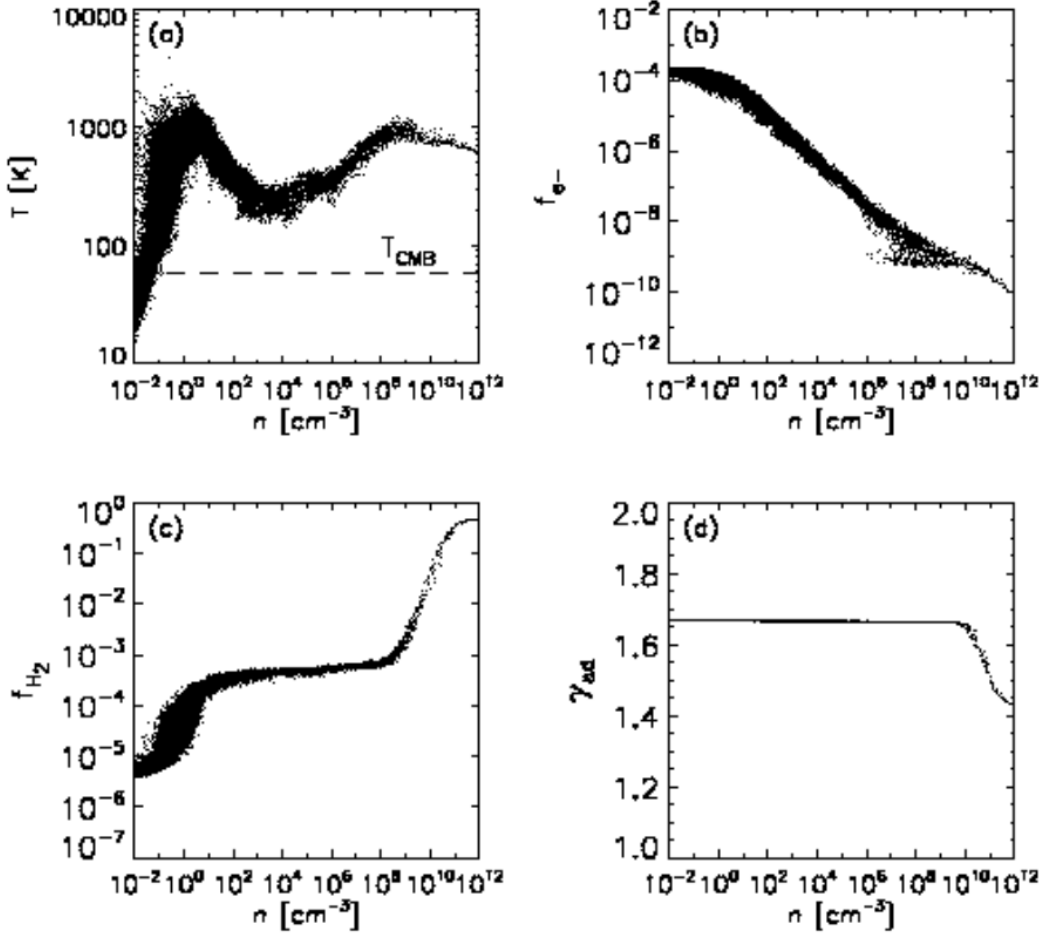


Figure 2. Physical state of the collapsing core. The situation is shown just prior to the formation of the first sink particle. (a) Temperature; (b) free electron fraction; (c) molecular hydrogen fraction; and (d) adiabatic exponent γ_{ad} vs. density. The gas that collapses into the minihalo is heated adiabatically to ~ 1000 K as it reaches $n \sim 1 \text{ cm}^{-3}$ (panel a). At this point f_{H_2} becomes high enough (panel c) to allow the gas to cool through H_2 rovibrational transitions to a minimum of $T \sim 200$ K, which is reached at $n \sim 10^4 \text{ cm}^{-3}$ (panel a). After the onset of gravitational instability, the gas reaches yet higher densities, and is heated to a maximum of ~ 1000 K once it approaches a density of $\sim 10^8 \text{ cm}^{-3}$. At this density three-body reactions become important, and the gas is rapidly converted into fully molecular form (panel c). The increased H_2 cooling rate then roughly equals the adiabatic heating rate, and thus the highest density gas is nearly isothermal. As the gas is transformed into molecular form, the equation of state changes as well so that γ_{ad} evolves from $5/3$ to approximately $7/5$ (panel d).

Other types of feedback also have the potential to halt protostellar accretion and set the upper mass limit of Pop III stars. McKee & Tan (2008) consider several feedback mechanisms operating during Pop III star formation, including H_2 photodissociation and $\text{Ly}\alpha$ radiation pressure. They find, however, that the accretion rate is not significantly reduced through feedback until HII region breakout beyond the gravitational escape radius, generally occurring once the star has reached $50\text{--}100 M_{\odot}$. Omukai & Inutsuka (2002), on the other hand, find that for spherically symmetric accretion onto an ionizing star, the formation of an HII region in fact does not impose an upper mass limit to Pop III stars. As McKee & Tan (2008) determine, however, this does not remain the case for rotating inflow.

This previous work shows that further considerations such as a time-dependent accretion rate and a non-spherical, disk-like geometry around the protostar (see also Tan & Mc-

Kee 2004) will be integral to fully determining the effects of protostellar feedback and will require study through three-dimensional calculations. We do not include any radiative feedback effects here, and thus our work represents a no-feedback limit of protostellar accretion onto a Pop III star. However, during the initial stages of protostellar growth, the feedback should be much weaker than in later stages when the star becomes more massive and luminous. As mentioned above, McKee & Tan (2008) estimate that the accretion rate is not significantly reduced until the Pop III star has gained $\sim 50 M_{\odot}$, and the rate of protostellar mass growth given by Bromm & Loeb (2004) indicates that such masses are not reached until $\sim 10^4$ yr after accretion begins. We thus end our calculation somewhat before this, after 5000 yr of accretion, before feedback effects have become too strong to ignore. Up until this point, our calculations should still give a good estimate of the geometry and possible fragmen-

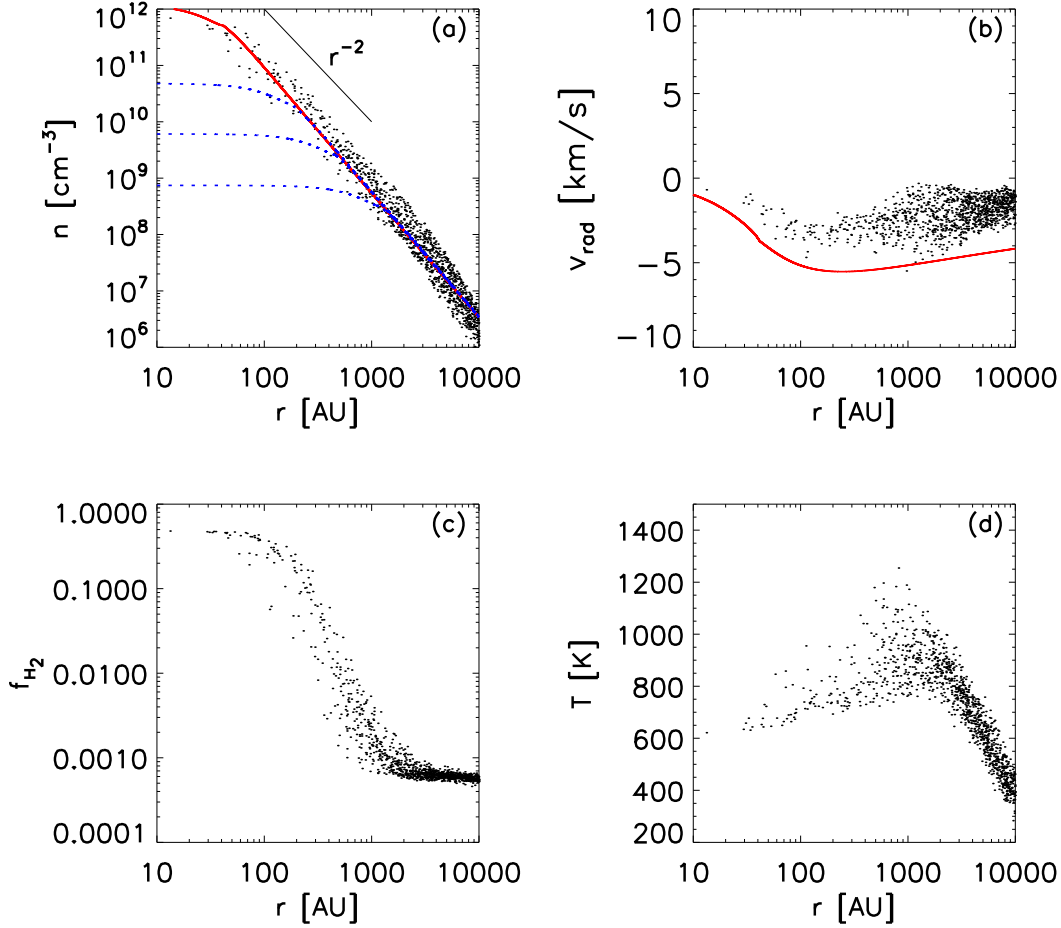


Figure 3. Initial collapse prior to the formation of the first sink particle. Shown are a number of variables as a function of radial distance from the density maximum. (a) Number density; (b) radial velocity; (c) molecule fraction; and (d) temperature vs. r . Also shown are the number density and radial velocity of a Larson-Penston type similarity solution for the equation of state $P = K\rho^\gamma$, where $\gamma = 1.09$ and $K = 4.2 \times 10^{11}$ (in cgs units), as in Omukai & Nishi (1998). The solid red lines (in panels a and b) represent the latest stage of collapse that was calculated, when the peak density is near 10^{12} cm^{-3} , while the dashed blue lines (in panel a) represent various earlier stages of collapse. Note that the analytical solution reproduces the density profile found in the numerical calculation very well. The velocity profile is also in reasonable agreement with the simulation, though, also as in Omukai & Nishi (1998), exhibiting a somewhat larger normalization due to differences in initial and boundary conditions.

tation of the prestellar core as well as the early protostellar accretion rate and its time dependence.

2.3 Chemistry, heating and cooling

The chemistry, heating and cooling of the primordial gas is treated in a fashion very similar to previous studies (e.g. Bromm & Loeb 2004; Yoshida et al. 2006). We follow the abundance evolution of H , H^+ , H^- , H_2 , H_2^+ , He , He^+ , He^{++} , e^- , and the deuterium species D , D^+ , D^- , HD , and HD^+ . We use the same chemical network as used in Johnson & Bromm (2006) and include the same cooling terms.

At densities greater than $\simeq 10^8 \text{ cm}^{-3}$, three-body processes gain importance. The reaction rates for



and



must be included (Palla et al. 1983). Because the gas is becoming fully molecular, in our cooling rates we furthermore account for enhanced cooling due to collisions between H_2 molecules. The heating rate due to H_2 formation heating is also included. Furthermore, the equation of state of the gas must be modified. More specifically, we adapt the adiabatic exponent γ_{ad} and the mean molecular weight μ to account for the increasing H_2 abundance f_{H_2} . These modifications for densities greater than 10^8 cm^{-3} are applied in the same way as described in Bromm & Loeb (2004), except for the modification of γ_{ad} , which is handled in the same way as described in Yoshida et al. (2006).

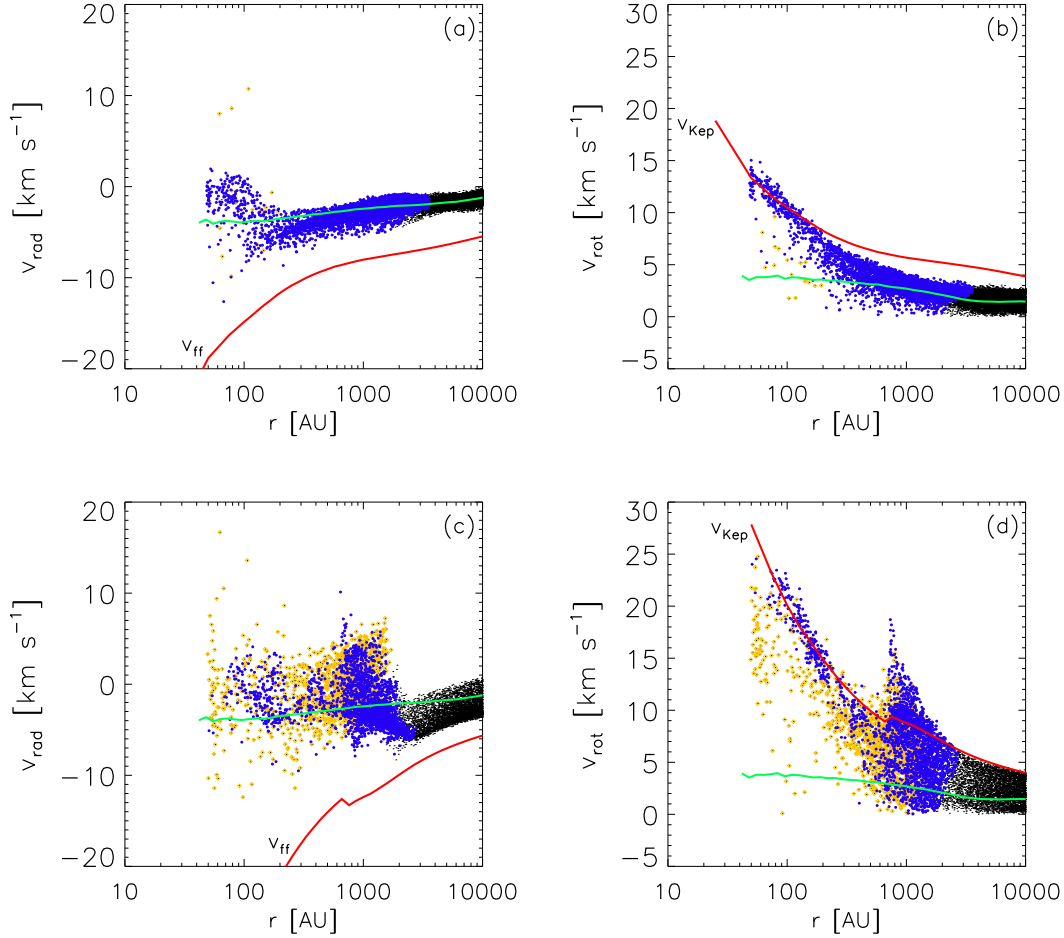


Figure 4. Kinematics around the main sink particle. (a) Radial velocity versus distance from the main sink at 250 yr after the initial sink formation. Colored particles are those with densities greater than 10^8 cm^{-3} - yellow diamonds are high-density heated particles with temperatures greater than 2500 K, and blue circles are high-density cool particles with temperatures less than 2500 K. The red line shows the gravitational free-fall velocity v_{ff} , determined using the enclosed mass within the given radius. For comparison to the physical situation at earlier times, the green line is the radially averaged radial velocity around the main sink immediately after it first forms. (b) Rotational velocity versus distance from the main sink at 250 yr after sink formation. Blue and yellow particles have the same meaning as in panel (a). The red line shows v_{Kep} , calculated using the enclosed mass. The green line is the radially averaged rotational velocity around the main sink immediately after it first forms. (c) Radial velocity versus distance from main sink at 5000 yr after initial sink formation. Notation is the same as in panel (a). (d) Rotational velocity versus distance from main sink at 5000 yr after initial sink formation. We adopt the same convention as in panel (b). Towards later times, the cold gas settles into a nearly Keplerian configuration.

3 NUMERICAL METHODOLOGY

3.1 Initial setup

We carry out our investigation using Gadget, a widely-tested three dimensional smoothed particle hydrodynamics (SPH) code (Springel et al. 2001; Springel & Hernquist 2002). Simulations are performed in a periodic box with size of $100 h^{-1} \text{ kpc}$ (comoving) and initialized at $z = 99$ with both DM particles and SPH gas particles. This is done in accordance with a ΛCDM cosmology with $\Omega_{\Lambda} = 0.7$, $\Omega_{\text{M}} = 0.3$, $\Omega_{\text{B}} = 0.04$, and $h = 0.7$. We use an artificially large normalization of the power spectrum, $\sigma_8 = 1.4$, to accelerate structure formation in our relatively small box.

A preliminary run with a modest resolution of $N_{\text{SPH}} = N_{\text{DM}} = 128^3$ allows us to locate the formation site of the first minihalo. Three refinement levels of length 40, 30, and

20 kpc (comoving) are subsequently added in this region, and particle positions are shifted so that this region will be in the center of the simulation box. Each level of higher refinement replaces particles from the lower level with eight child particles such that in the final simulation a parent particle is replaced by up to 512 child particles. The highest-resolution gas particles each have a mass $m_{\text{SPH}} = 0.015 M_{\odot}$, so that the mass resolution of the refined simulation is: $M_{\text{res}} \simeq 1.5 N_{\text{neigh}} m_{\text{SPH}} \lesssim 1 M_{\odot}$, where $N_{\text{neigh}} \simeq 32$ is the typical number of particles in the SPH smoothing kernel (e.g. Bate & Burkert 1997).

The size of the refinement levels had to be chosen carefully. The level of highest refinement must be large enough to encompass all the mass that will eventually become the first minihalo. If this level of highest refinement is too small, lower-resolution particles will drift into the center of the col-

lapsing region and disrupt the collapse of the high-resolution particles. Furthermore, there will be some artificial density enhancement for lower-resolution particles that are near the boundary of a higher-resolution region. This is because the particles of lower refinement levels have higher masses, and for a given density the corresponding smoothing length for lower-resolution particles should be larger than the smoothing length for higher-resolution particles. Smoothing lengths for particles of both resolutions will be very similar, however, if they are very close to each other. This causes low-resolution particles near a boundary to have artificially reduced smoothing lengths and overly enhanced densities. However, this will not pose a problem as long as the highest refinement level is large enough such that the low-resolution particles are well outside of the collapsing region of interest.

3.2 Sink particle creation

When the density of a gas particle becomes greater than $n_{\max} = 10^{12} \text{ cm}^{-3}$, this particle and the surrounding gas particles within a distance of less than the accretion radius r_{acc} are converted into a single sink particle. We set r_{acc} equal to the resolution length of the simulation, $r_{\text{acc}} = L_{\text{res}} \simeq 50 \text{ AU}$, where:

$$L_{\text{res}} \simeq 0.5 \left(\frac{M_{\text{res}}}{\rho_{\max}} \right)^{1/3},$$

with $\rho_{\max} \simeq n_{\max} m_{\text{H}}$. The sink particle's initial mass is close to the simulation's resolution mass, $M_{\text{res}} \simeq 0.7 M_{\odot}$.

Our density criterion for sink particle formation is robust even though we do not explicitly check that the sink region satisfied further criteria such as being gravitationally bound and not having rotational support. As discussed in Bromm et al. (2002), crossing the n_{\max} threshold is already equivalent to meeting these further criteria due to the runaway nature of the collapse. The average density of the disk (see Sec. 4.2.1) does not go above $\simeq 10^{10} \text{ cm}^{-3}$, and gas must collapse to densities two orders of magnitude higher before a sink is formed at the center of the infalling region. This along with our very small value for r_{acc} ensures that the particles that become sinks are indeed undergoing gravitational collapse. Furthermore, an examination of movies of the simulation shows that even the lowest-mass sinks are created only in pre-existing high-density clumps of gas that formed through gravitational instability, even though the clumps may no longer be clearly visible after the sink forms and accretes mass. During earlier test runs, however, using only the density criterion was problematic for other numerical reasons. This was because the larger sinks would contribute their high masses to the kernels of nearby gas particles, causing them to artificially jump to $n > 10^{12} \text{ cm}^{-3}$ and become sink particles themselves. These artificial sink particles had masses well below M_{res} . However, once we corrected this problem by removing all sink particles from the density calculation, all sinks that were formed had initial masses $\geq M_{\text{res}}$.

After a sink's formation, its density, temperature, and pressure are no longer evolved in time. Instead, their density is held constant at 10^{12} cm^{-3} . The temperature of the sinks is also held constant at 650 K, a typical temperature for gas reaching 10^{12} cm^{-3} , and the sinks are furthermore kept at

the pressure which corresponds to the above temperature and density. Giving the sink a temperature and pressure makes it behave more like a gas particle, and it furthermore prevents the existence of a pressure vacuum around the sink that would make the sink accretion rate artificially high (see Bromm et al. 2002; Martel et al. 2006). Changes in the sink's position, velocity, and acceleration due to gravitational interaction are still evolved, however, and as the sink accretes mass its gravity becomes the dominant force, and it gradually begins to act more like a non-gaseous N-body particle.

Once a sink particle is formed, all gas particles or other sink particles that cross within r_{acc} of the sink particle are removed from the simulation, and their mass is added to that of the sink particle. After each subsequent accretion event, as well as when the sink is initially formed, the position and velocity of the sink are set to be the mass-weighted average of the sink particle and the gas particles that it has accreted. The sink approximately represents the growing hydrostatic core, though its size, of order r_{acc} , is much larger than the true expected size of a core (e.g. Omukai & Nishi 1998).

The sink particle method has multiple advantages. It eliminates the need to include high density physics that becomes relevant only at $n > 10^{12} \text{ cm}^{-3}$. Furthermore, simulation timesteps become prohibitively small as the density increases, and representing a region of $n > 10^{12} \text{ cm}^{-3}$ with a single sink particle allows the mass flow into protostellar regions to be followed for many dynamical times without continuing to increasingly high densities and small timesteps. Instead of estimating the accretion rate from the instantaneous density and velocity profiles at the end of the simulation, as done in Abel et al. (2002) and Yoshida et al. (2006), the sink particle method allows the accretion history to be directly followed. Furthermore, without the sink particle method, finding multiple fragments would require that they form at very nearly the same time, such as the fragments in Turk et al. (2009) which formed only 60 years apart. Using sink particles allows for the study of fragmentation that occurs on significantly longer timescales than this.

4 RESULTS

4.1 Initial runaway collapse

Fig. 1 shows the final simulation output on various scales. The expected filamentary structure is apparent, and the first minihalo has formed in the central region where several filaments intersect by $z \simeq 20$. We measure the halo virialization radius r_{vir} as the point at which $\rho_{\text{DM}} = \rho_{\text{vir}} \equiv 200\rho_{\text{b}}$, where ρ_{DM} is the average halo DM density, ρ_{vir} is the DM density at the point of virialization, and ρ_{b} is the average background matter density at the time of halo virialization. We then find that $r_{\text{vir}} \simeq 90 \text{ pc}$ and $M_{\text{halo}} \simeq 2.6 \times 10^5 M_{\odot}$. The spin parameter $\lambda = J|E|^{1/2}/GM^{5/2}$ is approximately 0.13 for our halo, where J is the total angular momentum, E is the binding energy, and M is the total halo mass. For our minihalo λ is somewhat higher than the typical value of 0.05 (e.g. Barnes & Efstathiou 1987; Jang-Condell & Hernquist 2001). However, despite our enhanced value of σ_8 , the minihalo's characteristics are within usual range.

After the DM in the minihalo virializes, the gas continues to collapse. As shown in Fig. 2, the results of our

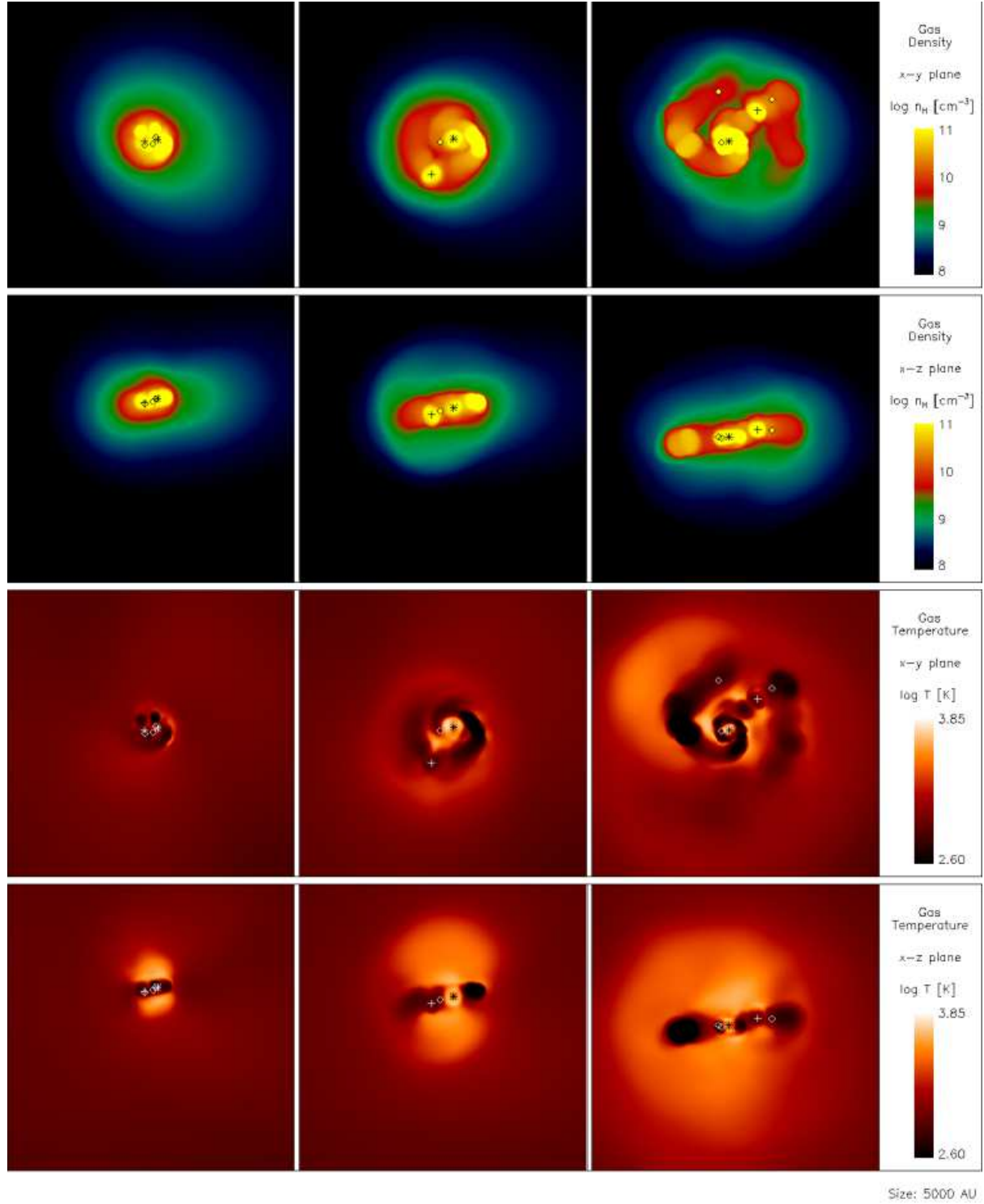


Figure 5. Density and temperature projections of the central 5000 AU. Each row shows the projections at 1000 yr (left), 2000 yr (center), and 5000 yr (right) after the initial sink formation. Asterisks denote the location of the most massive sink. Crosses show the location of the second most massive sink. Diamonds are the locations of the other sinks. *Top row* : Density structure of the central region in the $x-y$ plane. *Second row* : Density structure of the central region in the $x-z$ plane. *Third row* : Temperature structure of the central region in the $x-y$ plane. *Bottom row* : Temperature structure of the central region in the $x-z$ plane.

calculation up to the point of creation of the first sink particle agree well with previous studies (e.g. Bromm & Larson 2004; Yoshida et al. 2006). As expected, the gas heats adiabatically until reaching $n \sim 1 \text{ cm}^{-3}$, where it attains maximum temperatures of $\sim 1000 \text{ K}$. After this point the gas begins to cool through H_2 rovibrational transitions, reaching a minimum temperature of $T \sim 200 \text{ K}$ at a density of $n \sim 10^4 \text{ cm}^{-3}$. This is the density at which the gas reaches a quasi-hydrostatic ‘loitering phase’ (Bromm et al. 2002). After this phase the gas temperature rises again due to compressional heating until $n \sim 10^8 \text{ cm}^{-3}$, when three-body processes become important and cause the gas to turn fully molecular by $n \sim 10^{12} \text{ cm}^{-3}$ (see detailed discussion in Yoshida et al. 2006, 2008).

Fig. 3 shows the radial structure of the gas surrounding the density peak just before the first sink particle is created (compare with figure 2 in Bromm & Loeb 2004). The gas inside the central 100 AU has become almost fully molecular, and it evolves roughly isothermally due to the approximate balance between compressional and H_2 formation heating and enhanced H_2 cooling. The deviation from spherical symmetry of this central region is apparent in the ‘thickness’ of the radial profiles, particularly the profile of the H_2 fraction f_{H_2} . However, the gas density and velocity profiles still have the same general properties as those of the spherically symmetric Larson-Penston type similarity solutions, an example of which is shown in Fig. 3. The good agreement is evident, at least for the initial collapse phase. Omukai & Nishi (1998) used the same solution to describe their one-dimensional radiation-hydrodynamics simulations of primordial protostar formation. Though the velocities in the similarity solution are normalized to higher values, the velocities in our three-dimensional calculation exhibit very similar overall behavior, and the density profile matches the similarity solution especially well.

4.2 Protostellar accretion

4.2.1 Disk formation

We next discuss the transition from the quasi-spherical initial collapse towards a disk-like configuration. This transition is clearly visible in the velocity structure of the central region, which changes dramatically over the last several thousand years of the simulation as the disk-like nature of the central region becomes more apparent over time. In Fig. 4, we illustrate the evolution of the radial (left panels) and rotational velocity (right panels), measured with respect to the most massive sink. In comparing to the free-fall velocity, we calculate v_{ff} using the enclosed mass M_{enc} within a radial distance r from the main sink. At both times shown, 250 and 5000 yr after initial sink formation, pressure support from the central gas leads to a deviation from pure free fall, but the overall behavior of the radial velocity of the outer particles is similar to that of the v_{ff} profile. This is not the case for the particles very near the sink, however. The average radial velocity of the central gas particles, particularly the cold ones (shown in blue), approaches zero as the gas begins to exhibit more rotational motion.

The central region is evolving into a Keplerian disk ($v_{\text{rot}} \propto r^{-1/2}$) by just 250 yr after the first sink has formed. Note the comparison between the particle rotational veloci-

ties v_{rot} and the Keplerian velocity v_{Kep} (red line in Fig. 4), defined as

$$v_{\text{Kep}} = \sqrt{\frac{GM_{\text{enc}}}{r}}. \quad (5)$$

From Fig. 4 (panel b), it is apparent that the inner 100–200 AU of the disk are becoming rotationally supported ($v_{\text{rot}} \gtrsim v_{\text{Kep}}$) by 250 yr after sink formation. Despite some amount of rotational support, however, a fraction of the particles is still able to approach the sink, thus allowing continued accretion. After 5000 yr, the disk has grown to a radial size of slightly less than 2000 AU (panel c), while the cold disk particles exhibit nearly Keplerian motion (panel d). The spike at 700 AU (panel d) corresponds to a group of particles rotating around the second largest sink.

The assembly of the disk-like configuration around the first sink particle, and the subsequent fragmentation into additional sinks, are shown in Fig. 5. The growing disk is unstable and develops a pronounced spiral pattern, leading in turn to the formation of multiple high-density peaks. As is evident, regions of high density correlate with those of low temperature, due to the enhanced cooling there. The expanding, hour-glass shaped, bubble of hot gas (clearly visible in the bottom row) reflects the release of gravitational energy when particles fall into the deepening potential well around the central sink. The corresponding virial temperature is

$$T_{\text{vir}} \simeq \frac{GM_{\text{sink}}m_{\text{H}}}{k_{\text{B}}r_{\text{acc}}} \simeq 10^4 \text{ K},$$

where $M_{\text{sink}} \sim 10 M_{\odot}$. This gravitational source of heating causes the emergence of a hot gas phase around the central sink ($T \simeq 7,000 \text{ K}$), even in the absence of any direct radiative feedback from the protostar which is not included here. In Fig. 6, we illustrate the corresponding velocity field in two orthogonal planes at 5000 yr. The small infall velocities onto the disk and the high rotational, roughly Keplerian, velocities within the disk are apparent.

Fig. 7 shows the growth of the disk over time, where $t = 0 \text{ yr}$ marks the point at which the first sink forms. We estimate the disk mass by including all gas particles, sinks excluded, with a density greater than 10^8 cm^{-3} and a specific angular momentum within 50% of j_{Kep} , the specific angular momentum expected for a centrifugally supported disk, where $j_{\text{Kep}} = v_{\text{Kep}}r$. We here refer all velocities to the center of mass of the high-density ($n > 10^8 \text{ cm}^{-3}$) particles. In addition, we track the evolution of the mass in the ‘cool’ (dotted line) and ‘hot’ gas phase (dashed line), corresponding to temperatures less than 2500 K and greater than 2500 K, respectively. The mass of heated particles grows soon after the first sink is in place, whereas the cold component decreases as its mass is incorporated into the sinks or becomes part of the hot phase. Eventually what remains of the cold component is confined to the disk itself (see bottom two rows of Fig. 5).

The characteristics of the star-disk system in our simulation can be compared to the analytic predictions of Tan & McKee (2004). At a density and temperature of 10^8 cm^{-3} and 1000 K, respectively, we find a value of $K' \sim 1.33$ from their equation (7), where K' is the entropy parameter, defined by

$$K' = \frac{P/\rho^\gamma}{1.88 \times 10^{12} \text{ cgs}} = \left(\frac{T}{300 \text{ K}} \right) \left(\frac{n_{\text{H}}}{10^4 \text{ cm}^{-3}} \right)^{-0.1}. \quad (6)$$

We estimate that the total star-disk system mass (red line in Fig. 7) is $\sim 100 M_\odot$ at the end of our simulation and set ϵ_{*d} equal to 1 for the no feedback case, where ϵ_{*d} is the fraction of infalling mass that is able to reach the star-disk system without being diverted by protostellar outflows, again in the terminology of Tan & McKee. From their equation (8), we then calculate an expected accretion rate onto the star-disk system of $\lesssim 10^{-2} M_\odot \text{ yr}^{-1}$. In our simulation we find that over the 5000 yr of sink accretion, mass flows onto the star-disk system very steadily at approximately the same rate of $\sim 10^{-2} M_\odot \text{ yr}^{-1}$, which is also near the value for the average accretion rate onto the main sink particle (see Sec. 4.2.4). Fig. 7 further shows that once the first sink forms, the disk mass stays fairly constant at $\sim 35 M_\odot$ as mass falling from the outer regions onto the disk replaces the material accreted onto the sinks at similar rates.

Tan & McKee (2004) furthermore predict the time needed to build up a given stellar mass in their equation (9). If we assume a value of 1 for f_d , the ratio of disk to stellar mass, then the time to build up a $43 M_\odot$ star (the final mass of the main sink - see Sec. 4.2.4) is roughly 9000 yr. The simulation yields a similar though smaller value of 5000 yr, which reflects the slightly higher accretion rate of our simulation. Finally, if we estimate a value of 1 for f_{Kep} , the ratio of rotational to Keplerian velocity at the sonic point, then from equation (15) of Tan & McKee (2004) we find a predicted disk radius of $\sim 3000 \text{ AU}$. This value is also similar to the value of $\sim 2000 \text{ AU}$ found from the simulation.

4.2.2 Angular momentum evolution

How does the distribution of angular momentum change during the simulation? In Fig. 8, we demonstrate the increase in rotational support of the central region over time. Shown are the evolution of the enclosed mass (top panel), the specific angular momentum along the z -axis, j_z (middle panel), and the degree of rotational support (bottom panel). Here, rotational support is defined as

$$f_{\text{rot}} = \frac{j_z}{j_{\text{Kep}}}. \quad (7)$$

We determine j_z by averaging over all cool ($T < 2500 \text{ K}$) particles within small radial bins covering a total distance of 10^5 AU . Note how the inner $200 M_\odot$, corresponding to the central 10^4 AU , have spun up significantly in the process of disk formation. This occurs as the inner mass shells fall towards the center, leading to the increase in rotational support. The inner 200 AU of cool gas are fully rotationally supported by the end of the simulation (bottom panel).

To confirm that numerical viscosity is not a dominant factor in determining our results, we have compared the torque due to numerical viscosity ($\vec{\tau}_{\text{visc}}$) to those exerted by gravity and pressure ($\vec{\tau}_{\text{grav}}$ and $\vec{\tau}_{\text{pres}}$). The total torque on a given particle within a gas cloud is given by

$$\begin{aligned} \vec{\tau}_{\text{tot}} &= \vec{\tau}_{\text{grav}} + \vec{\tau}_{\text{pres}} + \vec{\tau}_{\text{visc}} \\ &= m_{\text{part}} \vec{r}_{\text{part}} \times (\vec{a}_{\text{grav}} + \vec{a}_{\text{pres}} + \vec{a}_{\text{visc}}), \end{aligned} \quad (8)$$

where \vec{r}_{part} is the distance of the particle from the center of the cloud, m_{part} the particle mass, and \vec{a}_{grav} , \vec{a}_{pres} and \vec{a}_{visc}

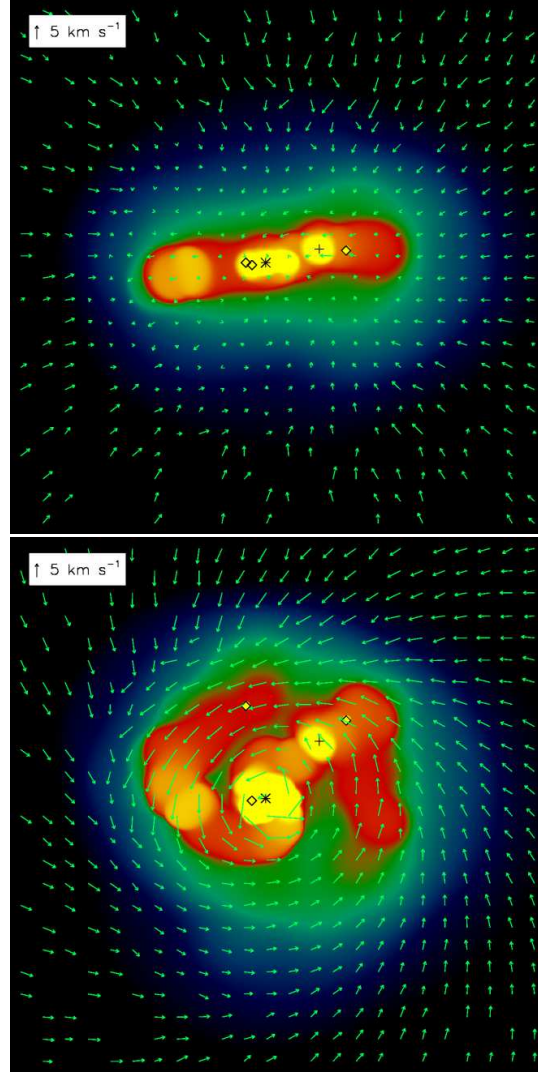


Figure 6. Velocity field of the central gas distribution. Sinks are denoted as in Fig. 5. *Top* : Density projection in the x - z plane after 5000 yr, shown together with the velocity field. Velocities are measured with respect to the center of mass of all $n > 10^8 \text{ cm}^{-3}$ particles. *Bottom* : Same as what is shown in the top panel except in the orthogonal (x - y) plane. It is evident how an ordered, nearly Keplerian velocity structure has been established within the disk.

are the accelerations due to gravity, pressure and viscosity, respectively. Similar to Yoshida et al. (2006), we store these accelerations for each particle and every timestep. We find that torques from gravity and pressure are dominant by an order of magnitude except in regions near the sinks. The viscous torques within $\sim 100 \text{ AU}$ of the sinks may exceed the gravitational and pressure torques at any given instant. However, unlike $\vec{\tau}_{\text{grav}}$ and $\vec{\tau}_{\text{pres}}$, $\vec{\tau}_{\text{visc}}$ near the sinks does not tend to continuously act in any preferred direction and thus averages out to be much smaller than the gravitational and pressure torques.

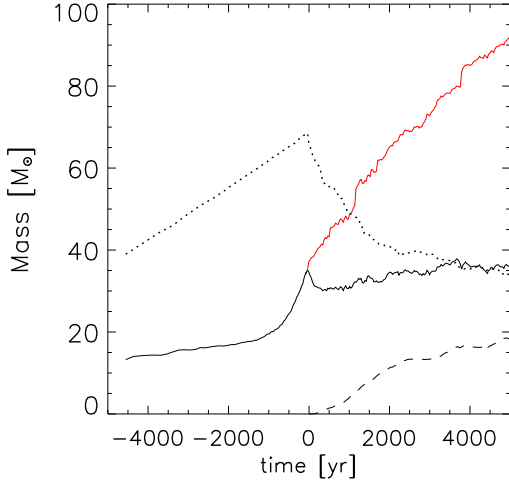


Figure 7. Disk mass vs. time since the creation of the first sink particle (solid line). Disk particles are considered to be all gas particles, excluding sinks, with density greater than 10^8 cm^{-3} and a specific angular momentum within 50% of j_{Kep} . Once the first sink forms at $t = 0$ yr, the red line shows the total mass of the star-disk system. Also shown is the total mass of $n > 10^8 \text{ cm}^{-3}$ particles (sinks excluded) with temperatures less than 2500 K (dotted line) and temperatures greater than 2500 K (dashed line).

sink	t_{form} [yr]	M_{final} [M_{\odot}]	r_{init} [AU]	r_{final} [AU]
1	0	43	0	0
2	300	13	60	700
3	3700	1.3	930	1110
4	3750	0.8	740	890
5	4400	1.1	270	240

Table 1. Formation times, final masses, and distances from the main sink. We include all sinks still present at the end of the simulation.

4.2.3 Binary and multiple formation

Around 300 yr after the first sink has formed, the disk becomes unstable to fragmentation and a second sink is created. We can estimate the value of Q in the Toomre criterion for disk gravitational instability,

$$Q = \frac{c_s \kappa}{\pi G \Sigma} < 1. \quad (9)$$

Here, Σ is the disk surface density and κ is the epicyclic frequency, which is equal to the angular velocity for Keplerian rotation. At this point in the simulation, the soundspeed c_s is approximately 3 km s^{-1} for a $\simeq 1000 \text{ K}$ disk, and $\kappa \simeq 3 \times 10^{-11} \text{ s}^{-1}$ for a disk with Keplerian rotation at the disk outer radius, which we take to be $R_{\text{disk}} \simeq 1000 \text{ AU}$. The disk mass is close to $30 M_{\odot}$, and $\Sigma \simeq M_{\text{disk}}/\pi R_{\text{disk}}^2 \sim 100 \text{ g/cm}^2$. This gives $Q \sim 0.4$, well-satisfying the fragmentation criterion.

Soon after the disk instability sets in, a pronounced spiral structure develops, as is evident in Fig. 5. The spiral perturbation serves to transport angular momentum outward through gravitational torques, allowing some of the inner gas

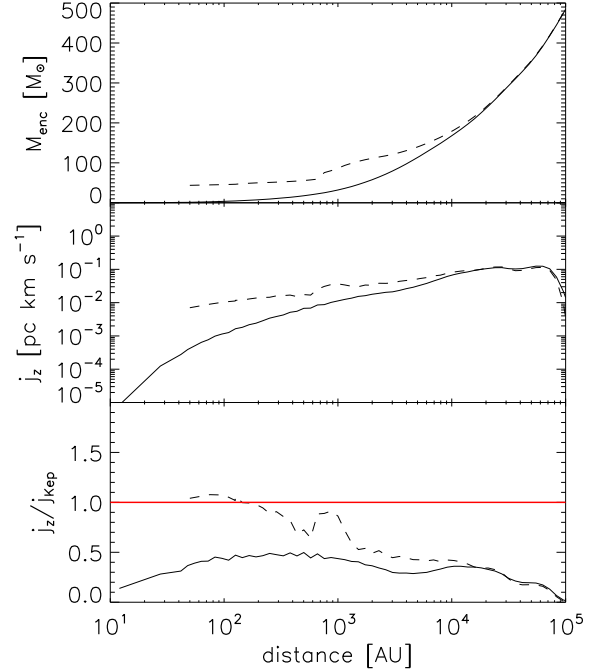


Figure 8. Angular momentum structure. *Top* : Enclosed mass versus distance from main sink particle at last simulation output before sink formation (solid line) and after 5000 yr of sink accretion (dashed line). *Middle* : Specific angular momentum j_z of the cool ($T < 2500 \text{ K}$) gas with respect to distance from the main sink at the same corresponding times. *Bottom* : Degree of rotational support of the cool gas. The solid red line shows where $j/j_{\text{Kep}} = 1$, the requirement for complete rotational support.

to accrete onto the sinks (see Krumholz et al. 2007). By 1000 yr after initial sink formation, several new fragments have formed, represented by new sink particles (shown in Fig. 5). Some of these fragments eventually merge with other more massive sinks, but by the end of our simulation we have 5 sink particles throughout the disk, described in Table 1. The two largest sinks are 700 AU apart, have a mass ratio of $\sim 1/3$, and form 300 yr apart (see Sec. 4.2.4 and Fig. 9). This is not unsimilar to the two fragments found in Turk et al. (2009), which had a separation of 800 AU, a mass ratio of $\sim 3/5$, and formed ~ 60 yr apart. The three smallest sinks in our calculation are all around $1 M_{\odot}$ and formed after approximately 4000 yr. Compared to the two largest sinks, these smaller sinks are quite low-mass and have been present in the simulation for only a short time. The two largest sinks seem to be the only long-term sinks in the simulation.

Protostellar feedback could reduce the number of fragments that form, since the initial protostar could heat the disk and inhibit further fragmentation, perhaps leaving a binary instead of a multiple system. This effect is shown in Krumholz et al. (2007), where the evolution of high-mass prestellar cores in the present-day Universe is simulated. They find that protostellar radiative feedback inhibits fragmentation and that the majority ($\gtrsim 90$ percent) of accreted stellar mass goes onto one protostar, though a small number of lower-mass stars can form at sufficiently large distances from the main protostar or in disk fragments formed through

Toomre instability. It will thus be important to include protostellar feedback in future simulations to fully ascertain the multiplicity of Pop III star formation.

4.2.4 Accretion rate

How do the initial hydrostatic cores develop into fully formed Pop III stars? Fig. 9 shows the growth of the two most massive sink particles over time. We find that the main sink approximately grows as $M \propto t^{0.55}$ (red line). By 5000 yr after sink formation, the main sink has grown to $43 M_{\odot}$, only slightly higher than the corresponding result from Bromm & Loeb (2004). The jumps in mass are instances where smaller sinks merged with the largest sink. One caveat to keep in mind is that we did not explicitly check that these smaller sinks were not centrifugally supported against infall towards the main sink before they were merged. However, we examined the largest secondary sink ($\sim 4 M_{\odot}$) that merged with the main sink. This merger occurred at 3700 yr after initial sink formation. We checked the secondary sink's specific angular momentum at the last simulation output before it merged with the main sink. At this time it was ~ 100 AU away from the main sink, and its specific angular momentum with respect to the main sink was $2 \times 10^{21} \text{ cm}^2 \text{ s}^{-1}$. This is less than the specific angular momentum required at this distance for centrifugal support against infall, $2.6 \times 10^{21} \text{ cm}^2 \text{ s}^{-1}$. It is thus plausible that this was indeed a true merger.

In Fig. 9, we also show the corresponding accretion rate onto the most massive sink particle over time (panel b). The accretion rate is highly variable and initially very large: $\dot{M} \sim 7c_s^3/G$, if we evaluate the sound speed at 700 K, and $\sim 50c_s^3/G$ at 200 K. These rates are similar to those predicted in analytic solutions (Larson 1969; Penston 1969; Shu 1977), and to the result found in Bromm & Loeb (2004). Note that the accretion rate does generally decline over time approximately as $\dot{M} \propto t^{-0.45}$, except for a few 'spikes' in accretion when the main sink merges with other smaller sinks. For comparison the accretion rate onto the second largest sink (dotted line) is also shown, whose powerlaw fit goes as $\dot{M} \propto t^{-0.39}$ (fit not shown) and is normalized to a value of about 1/5 that of the main sink. The lower rate is expected since the second largest sink accretes significantly cooler gas.

As accretion onto the main sink continues, the overall average accretion rate will drop to a much lower value, closer to the average value found in Bromm & Loeb (2004). If accretion were to continue for the entire lifetime of the star, 3×10^6 Myr, and if the accretion rate continued to decrease as approximately $\dot{M} \propto t^{-0.45}$, the final Pop III star would reach $M_* \lesssim 1000 M_{\odot}$. However, our fit likely overestimates the accretion rate at late times, and the actual final mass of the star is likely to be significantly lower. Furthermore, feedback effects will likely slow accretion, or even halt it entirely, before the star dies. Thus, our extrapolation serves as a robust upper limit to the final Pop III stellar mass.

4.2.5 Thermodynamics of accretion flow

After the initial sink particle has grown in mass, the surrounding gas divides into two phases - a hot and cold one. In Fig. 10, we illustrate this bifurcation with a temperature-density phase diagram at various stages of the simulation.

Heating becomes significant once the initial sink grows beyond $10 M_{\odot}$. At this mass the gravitational force of the sink particle is strong enough to pull gas towards it with velocities sufficiently high to heat the gas to a maximum temperature of $\sim 7,000$ K (see discussion in Sec. 4.2.1). This is the temperature where the collisional excitation cooling of atomic hydrogen begins to dominate over the adiabatic and viscous heating. The increasing mass of the sink causes a pressure wave to propagate outward from the sink and heat particles at progressively larger radii and lower density, as is visible in Fig. 5 and Fig. 10. The heated region extends out to $\sim 2,000$ AU at 5000 yr. The pressure wave thus propagates at a subsonic speed of $\sim 2 \text{ km s}^{-1}$.

The main sink is able to accrete a fraction of these heated particles (e.g. the yellow particle in Fig. 10), while it continues to accrete cold particles from the disk as well. We record the temperatures of the SPH particles accreted onto the sink, so that we can track the relative contributions from the two phases. When the main sink has grown to $\sim 30 M_{\odot}$, accretion from the hot phase begins to occur, such that heated particles contribute slightly over 50% to the total rate towards the end of the simulation. By this time, the average temperature of all particles accreted onto the main sink is close to 3000 K, a value indicative of significant contributions from the hot phase. The second-most massive sink, on the other hand, accretes particles from only the cool phase as it has not yet reached a sufficiently high mass to capture heated particles. It has, however, just become massive enough to begin heating its surrounding particles. Fig. 11 reveals the location of the two different gas phases in a complementary way by showing where cooling due to H_2 (left panel) and atomic hydrogen line cooling dominate (right panel). H_2 cooling is important in the cold, dense gas of the disk-like structure, whereas atomic cooling occurs in the hot, nearly spherical region around the largest sink particle. This region grows in size as the sink itself gains mass. By the end of the simulation, a similar heated region is also beginning to expand around the second-most massive sink.

Since the heated region is created by the sink particle's potential well, we can estimate its extent by evaluating the Bondi radius, which marks the distance out to where the gravitational energy of the sink will be greater than the thermal energy of the gas. If we use the final mass of the main sink, $M_{\text{sink}} \simeq 40 M_{\odot}$, and the maximum soundspeed of the gas particles, $c_s \simeq 7 \text{ km s}^{-1}$ for temperatures of 7000 K, we find

$$R_B \simeq \frac{GM_{\text{sink}}}{c_s^2} \simeq 750 \text{ AU} . \quad (10)$$

This is close to the size of the heated region seen in both Fig. 5 and Fig. 11. We should further note that, except for sink masses lower than $\sim 2 M_{\odot}$, R_B will be larger than r_{acc} , which is held constant at 50 AU. When the main sink reaches larger masses and begins to accrete heated particles, R_B is in fact over an order of magnitude larger than r_{acc} , indicating that our treatment of accretion is indeed conservative and that there is little un-physical accretion of heated particles.

4.2.6 Feedback

As noted earlier, the formation of a disk-like configuration around the protostar will have important implications for

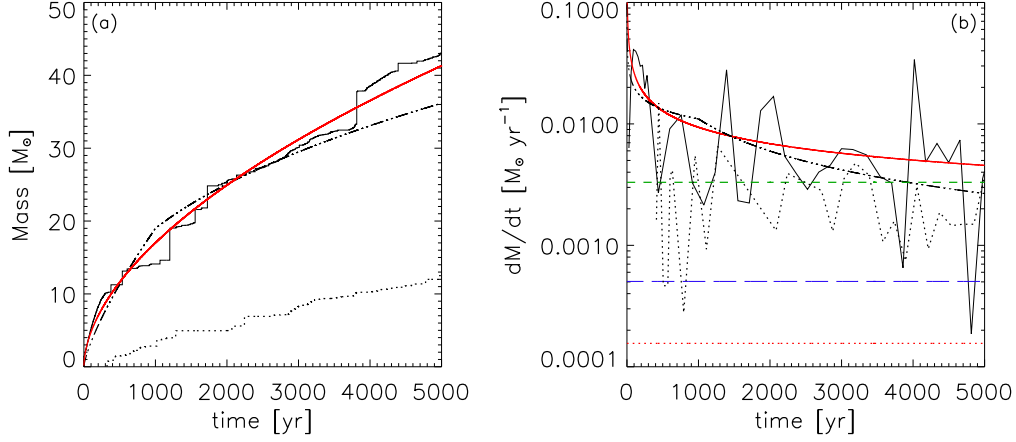


Figure 9. (a) Sink mass versus time since initial sink formation. The solid line shows the mass of the first sink particle over time in our calculation. The red line is the least-squares powerlaw fit to the sink mass over time, which goes as $M \propto t^{0.55}$. The dash-dotted line shows the result obtained by Bromm & Loeb (2004). The dotted line is the mass growth of the second largest sink. (b) Accretion rate versus time since initial sink formation. The solid line shows the accretion rate of the first sink particle throughout our calculation. The red line is the powerlaw fit to the mass accretion rate ($\dot{M} \propto t^{-0.45}$). The black dash-dotted line shows the instantaneous accretion rate found by Bromm & Loeb (2004), while the red dotted line is their average accretion rate over the lifetime of a Pop III star, determined by extrapolating their rate to 3×10^6 yr. The dotted line is the accretion rate of the second largest sink. Also shown are the Shu accretion rates for isothermal gas at 700 K (green short-dash line) and 200 K (blue long-dash line).

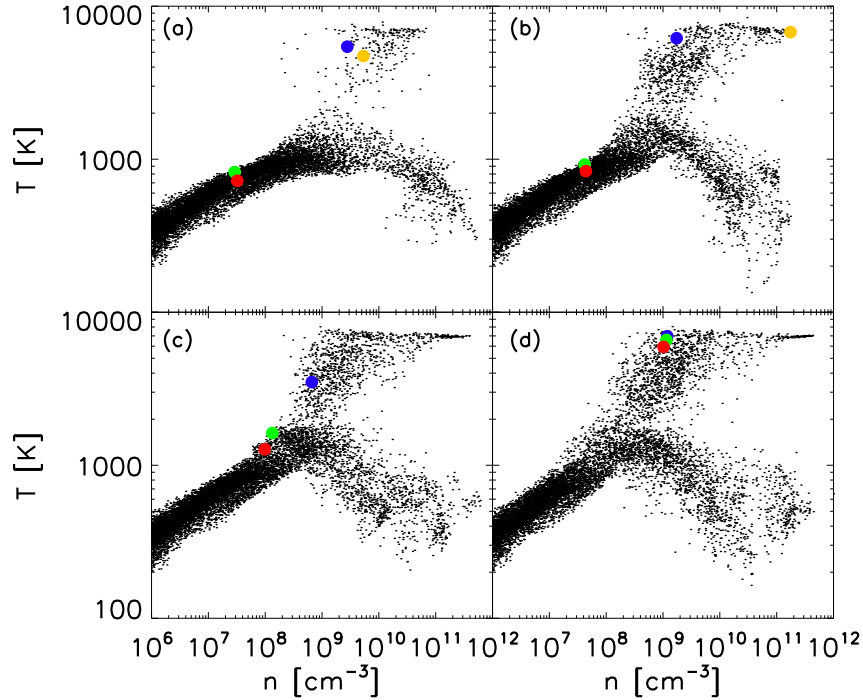


Figure 10. Evolution of thermodynamic properties. We plot temperature vs. number density at various times during the simulation. The colored dots trace the position of four representative particles, illustrating how the hot phase is populated. Note the hot particle that is accreted by the main sink *sim*2000 yr after the sink's creation (yellow dot). The times are as follows: (a) 1000 yr. (b) 2000 yr. (c) 3000 yr. (d) 5000 yr.

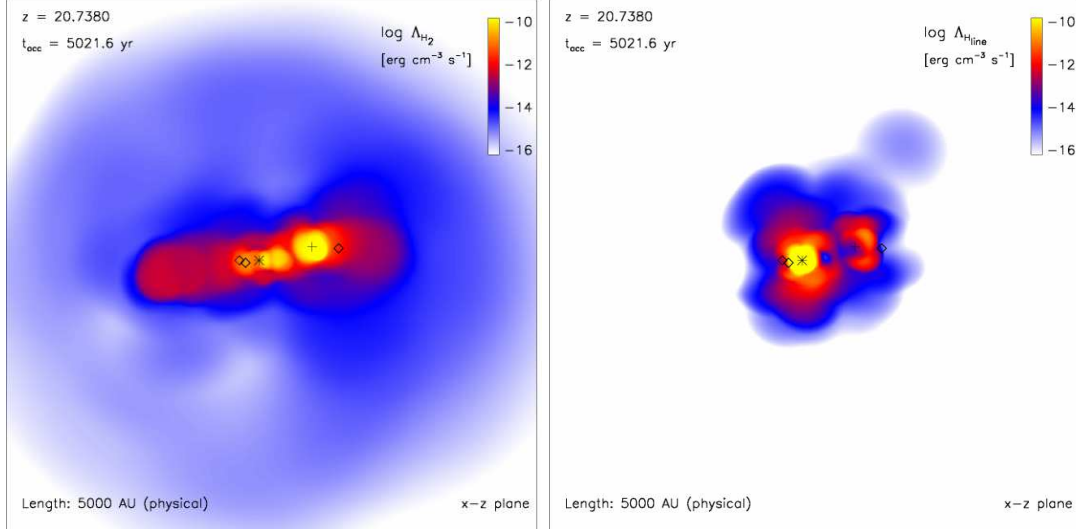


Figure 11. Dominant cooling processes in the center of the minihalo. Sinks are denoted as in Fig. 5. *Left* : H_2 cooling rate within the central 5000 AU, shown in projection along the x - z plane, after ~ 5000 yr of accretion. *Right* : H line cooling rate in the same region and at the same time, again shown in projection along the x - z plane.

feedback effects. As demonstrated by McKee & Tan (2008), the disk structure will mitigate the impact of protostellar feedback. Radiation will be able to escape along the polar directions, and although the innermost, optically thick, part of the accretion disk is not resolved in our simulation, it would shield a portion of the outer accretion flow from direct feedback. Future three-dimensional simulations that include radiative feedback will yield a better understanding of how and when disk accretion onto a primordial protostar may be terminated. We now wish to assess how important this neglected feedback would be up to the stage simulated here.

In Fig. 12, we compare the accretion luminosity, L_{acc} , with the Eddington luminosity due to electron scattering and due to H^- opacity. Determining L_{acc} requires an estimate of the protostellar radius R_* . In the initial adiabatic accretion phase, before Kelvin-Helmholtz contraction has commenced, the photospheric opacity of the protostar is dominated by H^- bound-free absorption (i.e., ‘Phase I’ of Omukai & Palla 2003). The extremely strong sensitivity of the H^- bound-free opacity to temperature ($\kappa_{\text{H}^-} \propto T^{14.5}$) locks the photospheric temperature to ~ 6000 K. We estimate that the protostar emits as a blackbody at this temperature and furthermore assume that the protostellar luminosity during this phase is dominated by L_{acc} . This is justified as long as $t_{\text{acc}} \lesssim t_{\text{KH}}$, where t_{acc} is the accretion timescale and t_{KH} the Kelvin-Helmholtz time. We then have

$$L_{*I} \simeq L_{\text{acc}} = \frac{GM_* \dot{M}}{R_*} = 4\pi R_*^2 \sigma_{\text{SB}} T^4, \quad (11)$$

where L_{*I} is the protostellar luminosity during the adiabatic accretion phase, σ_{SB} is the Stefan-Boltzmann constant, and $T = 6000$ K. This results in

$$R_{*I} \simeq 50 R_{\odot} \left(\frac{M_*}{M_{\odot}} \right)^{1/3} \left(\frac{\dot{M}}{\dot{M}_{\text{fid}}} \right)^{1/3}, \quad (12)$$

where R_{*I} is the protostellar radius during the adiabatic accretion phase, and $\dot{M}_{\text{fid}} \simeq 4.4 \times 10^{-3} M_{\odot} \text{ yr}^{-1}$, the fiducial accretion rate used by Stahler et al. (1986) and Omukai &

Palla (2003). Our simple estimate of how R_{*I} varies with mass and accretion rate is quite similar to the results of these more detailed previous studies, and here serves to highlight the relevant physics.

During the next phase, the protostellar radius begins to shrink due to Kelvin-Helmholtz contraction. The major source of opacity in the interior of the protostar is electron scattering, which is independent of density and temperature. This along with hydrostatic equilibrium yields the mass-luminosity relation $L_* \propto M_*^3$. Using figure 4 of Omukai & Palla (2003), we normalize this relation as follows:

$$L_{*II} \simeq 10^4 L_{\odot} \left(\frac{M_*}{10 M_{\odot}} \right)^3, \quad (13)$$

where L_{*II} is the protostellar luminosity during the Kelvin-Helmholtz contraction phase. If we further assume that $t_{\text{KH}} \simeq t_{\text{acc}}$, we arrive at

$$\frac{GM_*^2}{R_* L_*} \simeq \frac{M_*}{\dot{M}}. \quad (14)$$

Using $L_* \simeq L_{*II}$, we now find a relation for R_{*II} , the protostellar radius during the Kelvin-Helmholtz contraction phase:

$$R_{*II} \simeq 140 R_{\odot} \left(\frac{\dot{M}}{\dot{M}_{\text{fid}}} \right) \left(\frac{M_*}{10 M_{\odot}} \right)^{-2}. \quad (15)$$

In determining the evolution of L_{acc} , we set $R_* = R_{*I}$ at early times when the protostar is still experiencing adiabatic accretion. When $M_* \sim 10 M_{\odot}$, after approximately 800 yr of accretion, the value of R_{*II} falls below that of R_{*I} . At this point, we estimate that Kelvin-Helmholtz contraction has commenced and switch to setting $R_* = R_{*II}$. The resulting transition in the growth of L_{acc} can be seen in Fig. 12. The discontinuous slope in the accretion luminosity is an artefact of our approximate modelling of protostellar structure.

Since the accretion luminosity does not exceed either Eddington luminosity, we conclude that for the duration of

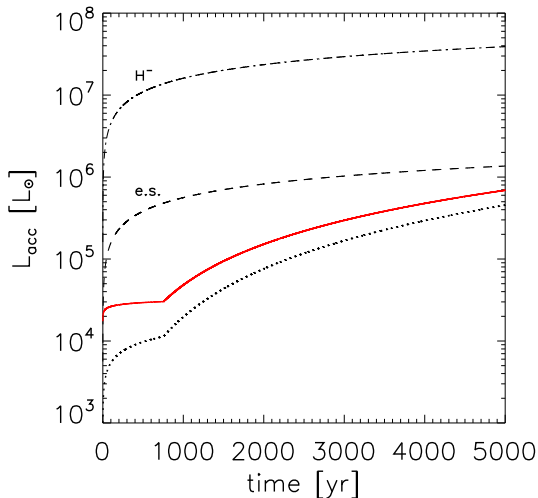


Figure 12. Impact of feedback on the accretion process. Solid red line is the accretion luminosity L_{acc} of the most massive sink versus time, calculated using $R_* = R_{*I}$ at early times and $R_* = R_{*II}$ at later times, as described in the text. In determining L_{acc} we use the power-law fit to the accretion rate ($\dot{M} \propto t^{-0.45}$). Dotted line is the prediction of L_{acc} by Tan & McKee (2004) given $f_d = 1$ and $K' = 1.33$. Dashed line is the Eddington luminosity L_{Edd} due to electron scattering, calculated using the sink mass. The dash - dotted line is L_{Edd} due to H^- bound-free opacity, calculated at a temperature of 6000 K. Note that the kink in the curves for the accretion luminosity is an artefact of our idealized modelling of protostellar structure.

our simulation, radiation pressure is not likely to significantly change the early accretion rates we have found. At later times, when the protostar reaches higher masses, however, and in particular when it reaches the ZAMS and hydrogen burning turns on, such feedback effects will become more important, and can no longer be neglected.

5 SUMMARY AND DISCUSSION

We have evolved a cosmological simulation until a primordial minihalo has formed at $z \simeq 20$, and follow the subsequent collapse of the gas in its center up to densities of $n = 10^{12} \text{ cm}^{-3}$. We find that the initial collapse, leading to the formation of a small hydrostatic core, is very similar to previous high-resolution work. Subsequently, a disk-like structure grows around the central core, eventually comprising a mass of $\sim 40 M_\odot$. We use the sink particle method to study the mass flow onto the central protostar for 5000 yr after its formation. Similar to the fragmentation found in Turk et al. (2009), we find that a second protostar forms soon after the first one. Upon further evolution, the disk exhibits spiral structure and undergoes further fragmentation, resulting in several more sink particles by the end of the simulation. Most of the mass of the smaller, secondary sinks is accreted through the disk, which consists mostly of cold gas. Once the main sink grows beyond $10 M_\odot$, its strong gravity is able to heat the surrounding particles to several thousand Kelvin, such that a two-phase medium emerges. The main sink is able to accrete these heated particles as well. After 5000 yr

of accretion, the most massive sink has reached $\sim 40 M_\odot$, at which point we terminate our simulation. Beyond this time, protostellar feedback effects, which are not included here, could no longer be neglected. The Pop III star, however, is expected to accumulate more mass. Even in the no-feedback case, however, the finite time available for accretion limits the Pop III mass to $\lesssim 1000 M_\odot$, where it is evident that in realistic settings, masses will not reach such extreme values. The accretion rate and the number of stars that form will be affected by protostellar feedback, with the likely outcome that both individual masses and the number of stars will be reduced (see Krumholz et al. 2007).

The recent radiation-hydrodynamical simulation by Krumholz et al. (2009), which studies the collapse of a massive pre-stellar core in a present-day GMC, shows interesting similarity to our investigation of the primordial case. They followed the collapse of a $100 M_\odot$ gas cloud, the formation of several protostellar seeds and their subsequent growth by accretion. Like our simulation, their system also evolved into a disk with a radius of order 1000 AU which fragmented due to gravitational instability. Similar to the sink mergers seen in our calculation, in their simulation the secondary stars that formed in the disk collided with the most massive star. By the end of their simulation, which was halted after $\sim 60,000$ yr, the system had evolved into a binary with stars of mass ~ 30 and $40 M_\odot$, masses fairly close to those of the two largest sinks in our simulation. Their calculation, however, included dust opacity as well as radiation pressure from the stars, and their initial conditions were typical of present-day star formation. Their accretion and fragmentation timescales were also much longer than those found in our calculation, but the overall qualitative results were alike.

Thus, the formation of binary and multiple systems within disk structures is likely not limited to modern-day star formation and can be found even in the primordial case, arising from cosmological initial conditions. Binary and multiple systems may be much more common in the Pop III case than previously thought. This is because most cosmological simulations do not follow the gas evolution for many years after the first protostar has formed, and fragmentation may not typically occur until after the simulations are stopped. For instance, the second protostar in our calculation did not form until 300 yr after the first, while the calculation of Turk et al. (2009) was stopped only 200 yr after the first protostar formed.

If Pop III binaries and multiples are actually common, then this has important implications for the final fate and observational signature of Pop III.1 stars, those zero-metallicity stars that have not yet been influenced by any previous stellar generation (e.g. Bromm et al. 2009). The presence of multiple accretors in our simulation did not seem to affect the accretion rate onto the largest sink as compared to previous work (Bromm & Loeb 2004). However, extending our simulation to later times might show that the most massive star would ultimately have to compete with its secondary companion for mass. As pointed out in Turk et al. (2009), if this in the end prevents the largest star from reaching very high masses ($\gtrsim 100 M_\odot$), this would also affect its resulting chemical signature. If multiple star formation were common in Pop III, then the occurrence of pair-instability supernovae (PISNe) might be significantly reduced, since stars that explode as PISNe must be in the higher mass

range ($140 M_{\odot} < M_{*} < 260 M_{\odot}$, Heger & Woosley 2002). Extremely metal-poor Galactic halo stars are believed to preserve the nucleosynthetic pattern of the first SNe, so this may help to explain the lack of PISNe chemical signatures found in halo stars (e.g. Christlieb et al. 2002; Beers & Christlieb 2005; Frebel et al. 2005; Tumlinson 2006; Karlsson et al. 2008). Turk et al. (2009) also note that if multiple high-mass Pop III stars can form within a minihalo at similar times, the ionizing flux on neighboring minihaloes could be increased, possibly leading to more efficient molecular cooling and ultimately lower-mass (Pop III.2) stars in the neighboring haloes (e.g. O’Shea et al. 2005). This again would influence the chemical signature of extremely metal-poor Galactic halo stars.

It should be mentioned that tight binaries on scales smaller than the resolution of our simulation could also form. Though a higher resolution study would be necessary to confirm this, the formation of a fragmenting disk of steadily increasing angular momentum in our cosmological simulation makes this a reasonable possibility. This could also limit the mass of Pop III stars, yielding similar effects on their resulting chemical signature as discussed above. The possible binary nature of Pop III stars, provided that they would not grow to become very massive, may also yield a direct primordial formation pathway to carbon-enhanced metal-poor (CEMP) stars, those metal-poor halo stars with unusually high carbon abundance (e.g. Frebel et al. 2007; Tumlinson 2007). If one of the members of a Pop III binary was an intermediate-mass star ($1 M_{\odot} \lesssim M_{*} \lesssim 8 M_{\odot}$), then the companion might undergo carbon enhancement through binary mass-transfer (e.g. Suda et al. 2004). This would occur when the intermediate-mass star enters an asymptotic giant branch (AGB) phase during which its C-rich ejecta can be captured by the companion. Furthermore, another type of Pop III signature would arise if gamma-ray bursts (GRBs) were able to form from very tight Pop III binaries. These may be detectable by *Swift* (see Bromm & Loeb 2006; Belczynski et al. 2007).

On the other hand, if both members of a typical Pop III binary were in the mass range to collapse directly into a black hole ($M_{*} \gtrsim 260 M_{\odot}$), then they could become massive black hole (MBH) binaries. Such a population of MBH binaries may emit a gravitational wave (GW) signature detectable by the future space-born *Laser Interferometer Space Antenna* (*LISA*). Previous studies have already explored the possibility of GW detection of MBH binaries formed through halo mergers during early structure formation (e.g. Wyithe & Loeb 2003; Sesana et al. 2005). Sesana et al. (2005) find that high redshift ($z \gtrsim 10$) MBH binaries with masses $\lesssim 10^3 M_{\odot}$ will be detectable by *LISA*. MBH binaries formed from Pop III progenitors thus approach the range of detectability by *LISA*, especially if the BHs continue to grow in mass through accretion. Furthermore, Belczynski et al. (2004) predict that advanced *LIGO* could also detect the GWs from Pop III MBH binary mergers. Madau & Rees (2001) suggested a different type of Pop III MBH signal when they discussed how an accreting primordial MBH could tidally capture a star and become a detectable off-nuclear ultraluminous X-ray source. They conclude, however, that such a non-primordial origin to Pop III binaries is extremely inefficient.

A modified picture of Pop III star formation is thus

emerging in which disk formation, fragmentation, and the resulting binary and multiple systems will play an important role in determining the mass of Pop III stars and their influence on later star and galaxy formation. Further studies, particularly ones which include protostellar feedback, will continue to add to this developing picture.

ACKNOWLEDGEMENTS

AS thanks Jarrett Johnson and Milos Milosavljevic for many helpful discussions. TG acknowledges support from the Heidelberg Graduate School of Fundamental Physics (HGSFP). The HGSFP is funded by the Excellence Initiative of the German government (grant number GSC 129/1). VB acknowledges support from NSF grant AST-0708795 and NASA ATFP grant NNX08AL43G. The simulations presented here were carried out at the Texas Advanced Computing Center (TACC).

References

- Abel T., Bryan G. L., Norman M. L., 2002, *Sci*, 295, 93
- Alvarez M. A., Bromm V., Shapiro P. R., 2006, *ApJ*, 639, 621
- Barkana R., Loeb A., 2001, *Phys.Rep.*, 349, 125
- Barnes J., Efstathiou G., 1987, *ApJ*, 319, 575
- Bate M. R., Burkert A., 1997, *MNRAS*, 288, 1060
- Beers T. C., Christlieb N., 2005, *ARA&A*, 43, 531
- Belczynski K., Bulik T., Heger A., Fryer C., 2007, *ApJ*, 664, 986
- Belczynski K., Bulik T., Rudak B., 2004, *ApJ*, 608, L45
- Bromm V., Coppi P. S., Larson R. B., 2002, *ApJ*, 564, 23
- Bromm V., Ferrara A., Coppi P. S., Larson R. B., 2001, *MNRAS*, 328, 969
- Bromm V., Kudritzki R. P., Loeb A., 2001, *ApJ*, 552, 464
- Bromm V., Larson R. B., 2004, *ARA&A*, 42, 79
- Bromm V., Loeb A., 2003, *Nat*, 425, 812
- Bromm V., Loeb A., 2004, *New Astron.*, 9, 353
- Bromm V., Loeb A., 2006, *ApJ*, 642, 382
- Bromm V., Yoshida N., Hernquist L., 2003, *ApJ*, 596, L135
- Bromm V., Yoshida N., Hernquist L., McKee C. F., 2009, *Nat*, 459, 49
- Christlieb N., Bessell M. S., Beers T. C., Gustafsson B., Korn A., Barklem P. S., Karlsson T., Mizuno-Wiedner M., Rossi S., 2002, *Nat*, 419, 904
- Ciardi B., Ferrara A., 2005, *Space Sci. Rev.*, 116, 625
- Frebel A., Aoki W., Christlieb N., Ando H., Asplund M., Barklem P. S., Beers T. C., Eriksson K., Fechner C., Fujimoto M. Y., Honda S., Kajino T., Minezaki T., Nomoto K., Norris J. E., Ryan S. G., 2005, *Nat*, 434, 871
- Frebel A., Johnson J. L., Bromm V., 2007, *MNRAS*, 380, L40
- Frebel A., Johnson J. L., Bromm V., 2009, *MNRAS*, 392, L50
- Glover S., 2005, *Space Sci. Rev.*, 117, 445
- Greif T. H., Johnson J. L., Bromm V., Klessen R. S., 2007, *ApJ*, 670, 1
- Haiman Z., Thoul A. A., Loeb A., 1996, *ApJ*, 464, 523
- Heger A., Woosley S. E., 2002, *ApJ*, 567, 532
- Hunter C., 1977, *ApJ*, 218, 834

- Jang-Condell H., Hernquist L., 2001, *ApJ*, 548, 68
- Johnson J. L., Bromm V., 2006, *MNRAS*, 366, 247
- Johnson J. L., Greif T. H., Bromm V., 2007, *ApJ*, 665, 85
- Karlsson T., Johnson J. L., Bromm V., 2008, *ApJ*, 679, 6
- Kashlinsky A., Rees M. J., 1983, *MNRAS*, 205, 955
- Kitayama T., Yoshida N., Susa H., Umemura M., 2004, *ApJ*, 613, 631
- Krumholz M. R., Klein R. I., McKee C. F., 2007, *ApJ*, 656, 959
- Krumholz M. R., Klein R. I., McKee C. F., Offner S. S. R., Cunningham A. J., 2009, *Sci*, 323, 754
- Larson R. B., 1969, *MNRAS*, 145, 271
- Machida M. N., Omukai K., Matsumoto T., Inutsuka S., 2008, *ApJ*, 677, 813
- Madau P., Ferrara A., Rees M. J., 2001, *ApJ*, 555, 92
- Madau P., Rees M. J., 2001, *ApJ*, 551, L27
- Martel H., Evans II N. J., Shapiro P. R., 2006, *ApJS*, 163, 122
- McKee C. F., Ostriker E. C., 2007, *ARA&A*, 45, 565
- McKee C. F., Tan J. C., 2002, *Nat*, 416, 59
- McKee C. F., Tan J. C., 2008, *ApJ*, 681, 771
- Miralda-Escudé J., 2003, *Sci*, 300, 1904
- Mori M., Ferrara A., Madau P., 2002, *ApJ*, 571, 40
- Norman M. L., O'Shea B. W., Paschos P., 2004, *ApJ*, 601, L115
- Omukai K., 2000, *ApJ*, 534, 809
- Omukai K., Inutsuka S.-i., 2002, *MNRAS*, 332, 59
- Omukai K., Nishi R., 1998, *ApJ*, 508, 141
- Omukai K., Palla F., 2003, *ApJ*, 589, 677
- O'Shea B. W., Abel T., Whalen D., Norman M. L., 2005, *ApJ*, 628, L5
- Palla F., Salpeter E. E., Stahler S. W., 1983, *ApJ*, 271, 632
- Penston M. V., 1969, *MNRAS*, 144, 425
- Ripamonti E., Haardt F., Ferrara A., Colpi M., 2002, *MNRAS*, 334, 401
- Saigo K., Matsumoto T., Umemura M., 2004, *ApJ*, 615, L65
- Schneider R., Ferrara A., Natarajan P., Omukai K., 2002, *ApJ*, 571, 30
- Sesana A., Haardt F., Madau P., Volonteri M., 2005, *ApJ*, 623, 23
- Shu F. H., 1977, *ApJ*, 214, 488
- Smith B. D., Sigurdsson S., 2007, *ApJ*, 661, L5
- Sokasian A., Yoshida N., Abel T., Hernquist L., Springel V., 2004, *MNRAS*, 350, 47
- Springel V., Hernquist L., 2002, *MNRAS*, 333, 649
- Springel V., Yoshida N., White S. D. M., 2001, *New Astron.*, 6, 79
- Stahler S. W., Palla F., Salpeter E. E., 1986, *ApJ*, 302, 590
- Tan J. C., McKee C. F., 2004, *ApJ*, 603, 383
- Tegmark M., Silk J., Rees M. J., Blanchard A., Abel T., Palla F., 1997, *ApJ*, 474, 1
- Tornatore L., Ferrara A., Schneider R., 2007, *MNRAS*, 382, 945
- Tumlinson J., 2006, *ApJ*, 641, 1
- Tumlinson J., 2007, *ApJ*, 665, 1361
- Turk M. J., Abel T., O'Shea B., 2009, *Sci*, 325, 601
- Wada K., Venkatesan A., 2003, *ApJ*, 591, 38
- Whalen D., Abel T., Norman M. L., 2004, *ApJ*, 610, 14
- Wytthe J. S. B., Loeb A., 2003, *ApJ*, 590, 691
- Yoshida N., Abel T., Hernquist L., Sugiyama N., 2003, *ApJ*, 592, 645
- Yoshida N., Omukai K., Hernquist L., 2008, *Sci*, 321, 669
- Yoshida N., Omukai K., Hernquist L., Abel T., 2006, *ApJ*, 652, 6